# High Resolution Sparse Imaging and Doppler Parameter Estimation of Fucheng-1 SAR Satellite

*CAI Fuxuan*[1,2], *ZHU Ziyi*[1,2], *SONG Yufan*[1,2], *BI Hui*[1,2*]

1. College of Electronic and Information Engineering, Nanjing University of Aeronautics and Astronautics, Nanjing 211106, P. R. China;

2. Key Laboratory of Radar Imaging and Microwave Photonics, Ministry of Education, Nanjing University of Aeronautics and Astronautics, Nanjing 211106, P. R. China

(Received 3 July 2025; revised 6 August 2025; accepted 20 August 2025)

**Abstract:** In recent years, the development of domestic commercial synthetic aperture radar (SAR) is in full swing, with multiple commercial SAR satellites in orbit, showing great potential in disaster monitoring, natural resource management and deformation observation. Fucheng-1 is the first C-band commercial SAR satellite for interferometric SAR (InSAR) service developed by Spacety China, which marks the gradual maturity of China's remote sensing data service. Based on the raw data collected by Fucheng-1, this paper firstly introduces the range-Doppler algorithm (RDA), then illustrates the parameter estimation method on the basis of fractional Fourier transform (FrFT) to realize the accurate estimation of azimuth chirp rate, which effectively improves imaging quality. Finally, the $L_1$-norm regularization based sparse imaging method is utilized to reconstruct images from down-sampled data. Experimental results show that the sparse imaging algorithm can accurately reconstruct the down-sampled Fucheng-1 data and suppress sidelobes and clutter.

**Key words**: Fucheng-1; synthetic aperture radar (SAR); sparse SAR imaging; parameter estimation

**CLC number**: TN957.52 **Document code**: A **Article ID**: 1005-1120(2025)04-0487-10

## 0 Introduction

Fucheng-1(Fig.1) is a C-band commercial synthetic aperture radar (SAR) satellite produced by Spacety China, which was launched from Jiu Quan Satellite Launch Center (Gansu Province, China) in June 2023. It can operate at stripmap, spotlight, scan and terrain observation by progressive scans (TOPS) mode with the maximum resolution of 0.5 m. Compared with previously launched satellites (Chaohu-1 and HISEA-1), Fucheng-1 provides interferometric SAR (InSAR) service[1], which can realize millimeter-level deformation monitoring of the ground surface. Partial basic parameters of the Fucheng-1 satellite are shown in Table 1.

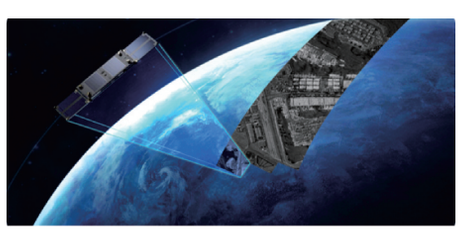

Fig.1 Fucheng-1 satellite

**Table 1 Parameters of Fucheng-1 satellite**

| Parameter | Value |
|---|---|
| Frequency/GHz | 5.4 |
| The maximum bandwidth/MHz | 300 |
| Altitude/km | 505 |
| Mass/kg | 300 |
| Inclination/(°) | 97.3 |
| Repeat time/d | 11 |
| Imaging width (stripmap)/km | 25 |

Many scholars have conducted research on the

*Corresponding author, E-mail address: bihui@nuaa.edu.cn.

**How to cite this article**: CAI Fuxuan, ZHU Ziyi, SONG Yufan, et al. High resolution sparse imaging and Doppler parameter estimation of Fucheng-1 SAR satellite[J]. Transactions of Nanjing University of Aeronautics and Astronautics, 2025, 42(4): 487-496.

http://dx.doi.org/10.16356/j.1005-1120.2025.04.005

data collected by Fucheng-1, and most of them focus on its interference ability. Feng et al.[2] used Fucheng-1 SAR images to analyze mining-induced subsidence in Karamay by InSAR Stacking and differential InSAR. Wu et al.[3] evaluated the surface deformation monitoring capabilities of Fucheng-1 satellite based on InSAR technique. Chang et al.[4] analyzed the deformation process of the landslide based on the SAR images, and showed more accurate monitoring results with a higher maximum detectable deformation gradient (MDDG) when compared to Sentinel-1. Xiao et al.[5] compared the deformation measurement capability of Lutan-1, Fucheng-1, and Hongtu-1. Liu et al.[6] detected thermal expansion and stress-induced deformations of towers under varying temperatures on the basis of differential interferograms from both ascending and descending Fucheng-1 data.

Sparse imaging algorithm is a technology to achieve efficient data acquisition and high-quality image reconstruction based on sparse signal characteristics, and its development process is closely related to the breakthrough of compressed sensing (CS) theory. The theory indicates a signal which is supposed to be compressible by a known transform can be accurately reconstructed with fewer measurements[7]. Hence, sparse SAR has great potential in achieving high-resolution and wide swath SAR imaging. In 2007, Baraniuk et al.[8] firstly introduced CS in the field of radar imaging and demonstrated its feasibility through simulation experiments. Herman et al.[9] proposed a method for sparse reconstruction of incoherent pulse signals using CS technology in 2008. In 2010, Potter et al.[10] conducted a comprehensive review of sparse SAR imaging and applied CS regularization methods to different radar fields. In 2012, Zeng et al.[11] proposed a novel imaging method based on $L_{1/2}$ regularization to reconstruct the scattering field, which optimizes a quadratic error term of the SAR observation process subject to the interested scene sparsity. Çetin et al.[12] provided an overview of CS based SAR imaging algorithms and emphasized their development prospects in various SAR application fields in 2014. In 2018, Ramdani et al.[13] improved SAR imaging methods based on CS theory by applying linear equations for system modeling and reconstructing sparse signals by a base tracking algorithm.

Although sparse SAR imaging theory has made significant progress, the problem of large computational complexity still needs to be addressed when processing large-scale data. In 2012, Zhang et al.[14] proposed a sparse SAR imaging azimuth distance decoupling algorithm based on $L_q$ norm regularization. Compared to traditional observation matrix-based algorithms, this algorithm applies simulation operators to directly perform sparse recovery in the data domain, solving the problem of high computational complexity in sparse SAR imaging and providing new possibilities for large-scale sparse reconstruction. In 2014, Yang et al.[15] introduced the matrix completion (MC) theory into SAR imaging, which eliminates the need to design complex measurement matrices for CS based imaging algorithms. In 2015, Zhang et al.[16] proposed a SAR moving target imaging algorithm based on sparse signal processing, which solves the phase error problem through phase recovery theory and achieves high-precision imaging. In 2018, Rouabah et al.[17] proposed a matching tracking algorithm, which could find sparse representations during compression and reconstruction processes. In 2020, Bi et al.[18] proposed a real-time sparse SAR imaging method, which effectively reduced the computational complexity, making real-time large-scale scene sparse reconstruction possible. In 2022, Xu et al.[19] combined the sparse inverse SAR (ISAR) imaging algorithm with a structured low-rank approach and applied the alternative direction method of multipliers (ADMMs) to effectively reduce the computational complexity. In 2023, Kang et al.[20] proposed an incremental SAR imaging approach based on the estimation of sensing dictionary matrix in the pursuit of sparsity. In 2024, Song et al.[21] presented a convolutional reweighted model based on structured sparsity features, which adaptively updated the imaging support set during the iteration process, aiming to reduce the data storage pressure. In 2025, Zhou et al.[22] put forward a deep equilibrium sparse SAR imaging method for compound regularization (CR-DEQ-

SAR), which could directly compute fixed points using analytical methods while maintaining constant memory requirements. In the same year, Kang et al.[23] proposed a novel approach based on an approximate version of an Omega-K algorithm without the Stolt interpolation, and the entire process could be efficiently carried out by a rapid matrix-vector multiplication operations. Among them, the sparse imaging method based on echo simulation operator has advantages in reducing complexity and improving calculation speed. In this paper, we apply the $L_1$-norm regularization based sparse imaging algorithm to raw data collected by Fucheng-1, thus demonstrating the effectiveness of the sparse imaging method based on echo simulation operator in real data.

In addition to SAR imaging methods, it is necessary to consider the influences caused by other issues. For example, SAR platform often deviate from the expected trajectory, which leads to azimuth phase error[24]. Azimuth phase error can lead to false target, defocus, and distortion in SAR images. Among them, the quadratic phase error (QPE) has the greatest influence on imaging quality[25]. The SAR autofocus technology is an effective means to overcome these problems by estimating and compensating phase error based on collected echo[26]. Map drift algorithm (MDA) can stably and efficiently retrieve the linear deformation rate of the surface, and is especially suitable for solving the scene where the traditional InSAR technology fails due to incoherence and atmospheric effects[27]. Phase gradient autofocus (PGA) utilizes the characteristics of strong scattering points in the image to estimate the derivative of the phase error and compensate the error after integration[28]. The energy of a linear frequency modulation (LFM) signal can be optimally concentrated after being processed by the fractional Fourier transform (FrFT) at its optimal order[29]. On this basis, FrFT has been introduced to SAR autofocus in recent years. In 2022, Li et al.[30] used a joint FrFT-WVD method to resist interference for bistatic forward-looking SAR system, especially for ship targets. In 2022, a 2-D-FrFT-based single-channel video-SAR imaging method was proposed to achieve well focused of moving targets[31]. Therefore, the parameter estimation method based on FrFT has giant potential in SAR field.

This paper is organized as follows. Section 1 introduces the range-Doppler algorithm (RDA). Section 2 demonstrates a parameter estimation method based on FrFT, and the imaging results are also given. Section 3 presents the $L_1$ sparse imaging algorithm based on RDA, and the reconstructed results of data collected by Fucheng-1 under the condition of 75% random down sampling are also presented. Finally, conclusions are reported in Section 4.

# 1 The Range-Doppler Algorithm

Since the data storage of Fucheng-1 satellite is based on committee on earth observation satellites (CEOS) structure, we can extract the complex echo data of interest area and key parameters of auxiliary processing from raw data files. Then, the focused imaging results can be obtained by appropriate imaging algorithm.

RDA was firstly put forward in 1976 to handle the data collected by SEASAT SAR, and then process the first airborne SAR image in 1979[32]. The algorithm decomposes two-dimensional processing into two one-dimensional operations, thus achieving the efficient modular processing, and it is still widely used. RDA can be divided into three steps, including range compression, range cell migration correction and azimuth compression.

## 1.1 Range compression

In the range direction, the pulse compression technology is used to compress the linear frequency modulation (LFM) signal transmitted by radar into narrow pulses, which can significantly improve the resolution in the range direction and effectively suppress noise interference. The required frequency domain filter is

$$H_{\mathrm{ra}}=\mathrm{rect}\left(-\frac{f_{\mathrm{r}}}{|K_{\mathrm{r}}|T}\right)\cdot\exp\left(-\mathrm{j}\pi\frac{f_{\mathrm{r}}^2}{K_{\mathrm{r}}}\right) \tag{1}$$

where $f_{\mathrm{r}}$ is range frequency, $K_{\mathrm{r}}$ range chirp rate, and $T$ pulse duration. After the multiplication of the data in range-Doppler domain with the filter $H_{\mathrm{ra}}$, the chirp signal is compressed into narrow pulses.

### 1.2 Range cell migration correction

Range migration is a phenomenon that the target echo changes with time in range direction and azimuth direction due to the relative motion between radar and target in SAR imaging. An effective solution is to apply interpolation processing correction in range-Doppler domain based on sinc function.

The range migration momentum to be corrected is

$$\Delta R = \frac{\lambda^2 R(\eta) f_\eta^2}{8 V_r^2} \tag{2}$$

where $\lambda$ is signal wavelength, $f_\eta$ azimuth frequency, $R(\eta)$ slant range, and $V_r$ effective radar velocity. After the interpolation, the distance migration curve is corrected to the same distance unit.

### 1.3 Azimuth compression

Similar to range compression, the azimuth resolution is improved by focusing the data with matched filter, which can be expressed as

$$H_{az} = \exp\left(-\mathrm{j}\pi \frac{f_\eta^2}{K_a}\right) \tag{3}$$

where $K_a$ is azimuth chirp rate. The azimuth chirp rate varying with the distance in the front side view can be generally calculated by

$$K_a = -\frac{2V_r^2}{\lambda R(\eta)} \tag{4}$$

The focused image can be obtained after completing the above three steps.

## 2 FrFT Based Parameter Estimation

Due to issues such as orbit error and attitude deviation in spaceborne SAR, the azimuth chirp rate calculated by Eq.(4) is not accurate enough to correct quadratic phase error, resulting in defocusing. In this part, we introduce a parameter estimation method based on FrFT to attain accurate azimuth chirp rate.

The fractional Fourier transform opens up a new fractional domain between the time domain and the frequency domain, which can effectively analyze non-stationary signals and linear time-varying systems, and the chirp signal is a typical non-stationary signal. The characteristic function definition of FrFT is

$$F^\alpha[\phi_n(t)] = \mathrm{e}^{-\mathrm{j}n\alpha}\phi_n(u) \tag{5}$$

where $F^\alpha$ is FrFT operator with rotation angle $\alpha$, $\alpha = \frac{\pi}{2}p$ the angle of rotation, and $p$ the order.

Under the FrFT with specific parameters, the chirp signal becomes a pulse function, making it easy to detect. The following describes the process of azimuth chirp rate estimation based on FrFT.

### 2.1 Range block and intensity point estimation

Considering the range-variant characteristics of azimuth chirp rate, it is necessary to block the echo data of the large scene in the range direction, so as to process each block separately and obtain the azimuth chirp rate estimation value in the range unit.

After range block, we can estimate the azimuth chirp rate of each range block. Firstly, perform an FrFT with angle $\alpha$ on the azimuthal signals $x(\eta)$ containing strong scattering points in each distance block data

$$u(k) = F^\alpha[x(\eta)] \tag{6}$$

Subsequently, using the entropy of the fractional Fourier domain signal $u(k)$ as the objective function, the optimal FrFT rotation angle can be obtained through gradient descent. The entropy of $u(k)$ is

$$I(\alpha) = \sum_{k=1}^{N} \frac{u^*(k)u(k)}{S} \ln \frac{S}{u^*(k)u(k)} \tag{7}$$

where $S = \sum_{k=1}^{N} u^*(k)u(k)$ is the energy of $u(k)$. The rotation angle $\alpha^{(n)}$ of the $n$th iteration is updated to

$$\alpha^{(n+1)} = \alpha^{(n)} - \gamma^{(n)} \cdot \frac{\partial I(\alpha^{(n)})}{\partial \alpha^{(n)}} \tag{8}$$

where $\gamma^{(n)}$ is the update step size determined by the Armijo criterion.

The specific contents of key steps are as follows. The concrete expression of FrFT operator with rotation angle $\alpha$ is

$$F^\alpha = K_\alpha(t,u) = \sum_{n=0}^{N-1} \exp(-\mathrm{j}n\alpha) \cdot H_{n,1}(u) \cdot H_{n,1}(t) \tag{9}$$

where $H_{n,\sigma}(x)$ is a Hermite-Gaussian function of or-

der $n$ and variance $\sigma$

$$H_{n,\sigma}(x)=\frac{1}{2^n n!\sqrt{\pi}\,\sigma}\cdot h_n\left(\frac{x}{\sigma}\right)\cdot\exp\left(-\frac{x^2}{2\sigma^2}\right) \tag{10}$$

where $h_n\left(\frac{x}{\sigma}\right)$ is Hermite polynomial of order $n$. In Eq.(9) the variance $\sigma$ is 1.

The operator $F^{\alpha}$ can be decomposed into features, which is expressed as

$$F^{\alpha}=\boldsymbol{V}\boldsymbol{D}\boldsymbol{V}^{\mathrm{H}} \tag{11}$$

where $\boldsymbol{V}$ is Hermite-Gaussian function matrix and $\boldsymbol{D}$ eigenvalue diagonal matrix, expressed as

$$\boldsymbol{D}=\mathrm{diag}\{\mathrm{e}^{0},\mathrm{e}^{-\mathrm{j}\alpha},\mathrm{e}^{-\mathrm{j}2\alpha},\cdots,\mathrm{e}^{-\mathrm{j}(N-1)\alpha}\} \tag{12}$$

In order to get the update of rotation angle $\alpha^{(n)}$, it is necessary to get the first derivative of $I(\alpha)$ to $\alpha$, which can be expressed as

$$\frac{\partial I(\alpha)}{\partial\alpha}=-\frac{1}{S}\sum_{k=1}^{N}\left\{\frac{\partial p(k)}{\partial\alpha}\ln p(k)+\frac{\partial p(k)}{\partial\alpha}\right\} \tag{13}$$

where $p(k)=u^{*}(k)u(k)$. The first derivative of $p$ to $\alpha$ is

$$\frac{\partial p}{\partial\alpha}=(\boldsymbol{V}\boldsymbol{Q}\boldsymbol{D}\boldsymbol{V}^{\mathrm{H}}\boldsymbol{x})^{*}\circ(\boldsymbol{V}\boldsymbol{D}\boldsymbol{V}^{\mathrm{H}}\boldsymbol{x})+(\boldsymbol{V}\boldsymbol{D}\boldsymbol{V}^{\mathrm{H}}\boldsymbol{x})^{*}\circ(\boldsymbol{V}\boldsymbol{Q}\boldsymbol{D}\boldsymbol{V}^{\mathrm{H}}\boldsymbol{x}) \tag{14}$$

where $\boldsymbol{Q}=\mathrm{diag}\{0,-\mathrm{j}1,-\mathrm{j}2,\cdots,-\mathrm{j}(N-1)\}$. The FrFT rotation angle $\alpha$ is updated to

$$\alpha=\alpha-\gamma^{(n)}\cdot\frac{\partial I(\alpha)}{\partial\alpha} \tag{15}$$

The Armijo criterion is a stopping condition of one-dimensional search. Under the given constants $\beta\in(0,1)$ and $\sigma\in(0,0.5)$, let the step factor $\gamma=\beta^{m}$, where $m$ is the smallest nonnegative integer satisfying

$$I(\alpha+\beta^{m}d)\leqslant I(\alpha)+\sigma\beta^{m}g^{\mathrm{T}}d \tag{16}$$

where $d$ represents the descending direction of the function at iteration point $\alpha$, and $g^{\mathrm{T}}$ the negative direction of the objective function gradient.

### 2.2 Doppler rate error calculation and linear fitting

After obtaining the updated rotation angle $\alpha$, it is necessary to calculate the Doppler frequency modulation error. The corresponding relationship between the chirp rate $K$ and the rotation angle $\alpha$ of FrFT is

$$K=-\cot(\alpha/2) \tag{17}$$

With the method of discrete scaling normalization, the estimated value of the corresponding Doppler frequency modulation error is

$$\Delta K_{\mathrm{a}}=-\frac{\cot\alpha}{N_{\mathrm{a}}}\cdot\mathrm{PRF}^{2} \tag{18}$$

where $N_{\mathrm{a}}$ is azimuth sampling points and PRF pulse repetition frequency.

The estimated azimuth chirp rate is linearly fitted by random sample consensus (RANSAC) algorithm, and the azimuth matched filter is updated to

$$H_{\mathrm{az}}^{(n)}=\exp\left(-\mathrm{j}\frac{\pi}{\hat{K}_{\mathrm{a}}}f_{\eta}^{2}\right) \tag{19}$$

where $\hat{K}_{\mathrm{a}}$ is the estimated azimuth chirp rate obtained by fitting the RANSAC algorithm.

Based on the above steps, a more accurate azimuth chirp rate can be obtained to improve the imaging quality.

### 2.3 Experimental results

In this paper, we select one scene data as an example, which is collected by Fucheng-1 satellite in Sanmen Bay, China, on April 11th, 2024. Main parameters of the selected scene are shown in Table 2.

**Table 2 Main parameters of the selected scene**

| Parameter | Value |
|---|---|
| Bandwidth/MHz | 200 |
| Range sampling frequency/MHz | 240 |
| Pulse duration/μs | 26.8 |
| PRF/Hz | 4 105 |
| Velocity/(m·s$^{-1}$) | 7 611 |

Fig.2 shows the azimuth chirp rate of whole raw data calculated by Eq.(4) and estimated by FrFT, respectively. Fig.3 shows the imaging results based on two kinds of azimuth chirp rate. In Fig.2, the calculated azimuth chirp rate is higher than the estimated one, as the variation of the slant range is small compared with the overall slant range, it seems close to linear variation, but the difference between them is not a constant. Fig.3 shows partially imaging results, and it can be clearly seen that the imaging result employing an estimated azimuth chirp rate has better focusing effects.

To clearly show the focusing quality when applying the estimated azimuth chirp rate, we com-

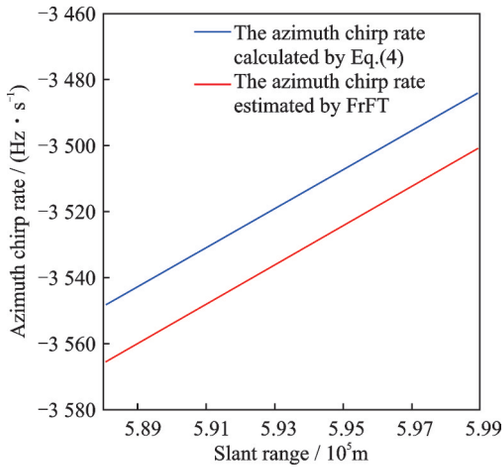


Fig.2 Two kinds of azimuth chirp rate varying with slant range

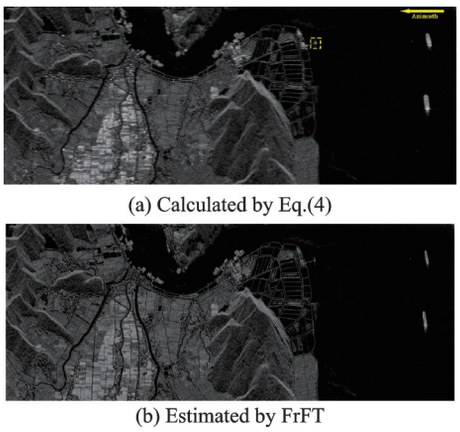

(a) Calculated by Eq.(4)

(b) Estimated by FrFT

Fig.3 Imaging results using different chirp rates

pare the azimuth response functions with different chirp rates, as shown in Fig.4, and the selected point is marked in Fig.3(a). It can be seen that the result produced by the estimated parameter maintains an ideal azimuth resolution.

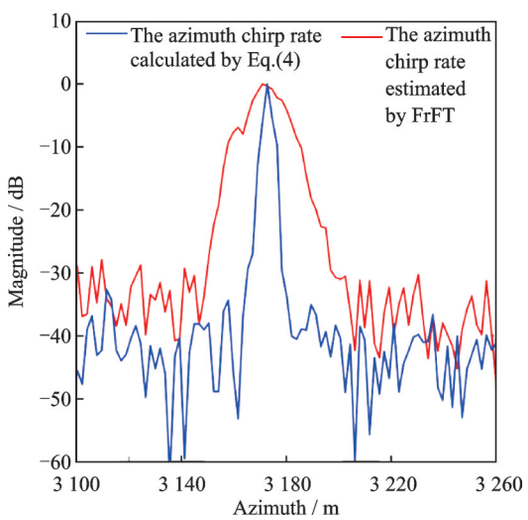


Fig.4 Azimuth response function with different azimuth chirp rates

Furthermore, in order to measure the imaging quality of the presented image, the concepts of image entropy and image contrast are introduced.

Image entropy is an important index to measure the complexity and uncertainty of an image. For SAR images with the size of $m\times n$, where $m$ is the number of azimuth points and $n$ the number of range points, let $I(i,j)$ represent the intensity of the point, where $i$ and $j$ represent azimuth and range sampling point index, respectively, and the image entropy can be expressed as

$$H=-\sum_{i=1}^{m}\sum_{j=1}^{n}\frac{|I(i,j)|^2}{D}\ln\left(\frac{|I(i,j)|^2}{D}\right) \tag{20}$$

where $D=\sum_{i=1}^{m}\sum_{j=1}^{n}|I(i,j)|^2$ denotes the total energy of image. Low image entropy corresponds to well focusing.

The image contrast is used to quantify the difference of scattering intensity in the interest area. Because of the multiplicative speckle noise in SAR images, traditional contrast calculation methods (such as directly calculating variance) may not be applicable. We adopt the coefficient of variation (CV) method to make the comparison, which can be expressed as

$$\mathrm{CV}=\frac{\sigma}{\mu} \tag{21}$$

where $\sigma$ is the standard deviation of the selected area, and $\mu$ the mean value. A high CV value indicates high quality of the image. The entropy and contrast of two images shown in Fig.3 are calculated in Table 3. As shown, Fig.3(b) has lower entropy and higher contrast when compared with Fig.3(a), which indicates its better image quality.

**Table 3 Entropy and contrast of images**

| Figure | Entropy | Contrast |
|---|---|---|
| Fig.3(a) | 0.296 9 | 6.096 1 |
| Fig.3(b) | 0.293 2 | 8.822 0 |

In order to further demonstrate the imaging results, we extract a large-scale data to process. The imaging result is shown in Fig.5.

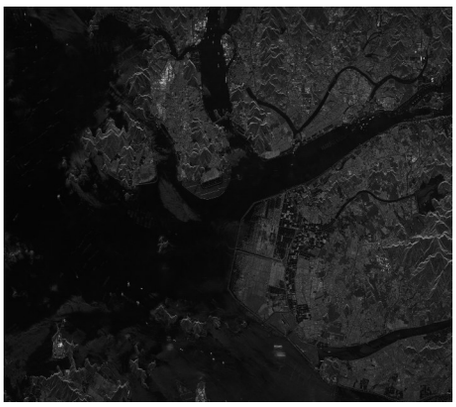

Fig.5 Large-scale imaging result

## 3 Sparse SAR Imaging

### 3.1 $L_1$-norm regularization based sparse imaging

In the sparse SAR system, sparse signal processing methods can utilize the sparse prior information of the scene, break through the theoretical limitations of traditional algorithms, and achieve significant improvements in data volume and resolution.

Assuming that two equally sized complex domain matrices $\boldsymbol{X}$ and $\boldsymbol{Y}$, representing the backscattered coefficient of the surveillance region and echo data, respectively. Then the approximated observation based sparse SAR imaging model can be expressed as[33]

$$\boldsymbol{Y}=\boldsymbol{\Theta}_{\mathrm{a}}H(\boldsymbol{X})\boldsymbol{\Theta}_{\mathrm{r}}+\boldsymbol{N} \tag{22}$$

where $\boldsymbol{\Theta}_{\mathrm{a}}$ and $\boldsymbol{\Theta}_{\mathrm{r}}$ are the down-sampling matrices in the azimuth and range directions, respectively; $\boldsymbol{N}$ is the system thermal noise, and $H(\cdot)$ the inverse imaging operators of MF-based algorithm expressed as

$$H(\boldsymbol{X})=M_{\mathrm{ra}}^{-1}(C^{-1}(M_{\mathrm{az}}^{-1}(\boldsymbol{X}))) \tag{23}$$

where $M_{\mathrm{ra}}^{-1}$ and $M_{\mathrm{az}}^{-1}$ denote the inverse operations of range and azimuth compression, respectively; and $C^{-1}$ is the inverse process of range cell migration correction.

For the model in Eq.(22), the considered scene can be reconstructed by solving the $L_1$-norm regularization problem as

$$\hat{\boldsymbol{X}}=\arg\min_{\boldsymbol{X}}\left\{\|\boldsymbol{Y}-\boldsymbol{\Theta}_{\mathrm{a}}H(\boldsymbol{X})\boldsymbol{\Theta}_{\mathrm{r}}\|_{\mathrm{F}}^{2}+\beta\|\boldsymbol{X}\|_{1}\right\} \tag{24}$$

where $\hat{\boldsymbol{X}}$ is the reconstructed image of a 2-D considered scene, and $\beta$ the regularization parameter.

For solving the problem shown by Eq.(24), this paper lists the iterative soft thresholding (IST) algorithm detailed in Table 4, where $k$ denotes the sparsity level, $|\cdot|_{k+1}$ the $(k+1)$th maximum element, and $R(\cdot)$ the thresholding functions expressed as

$$R(x)=\begin{cases}\mathrm{sign}(x)(|x|-\beta\mu) & |x|\geqslant\beta\mu\\ 0 & \text{otherwise}\end{cases} \tag{25}$$

where $\mu$ influences the convergence speed.

**Table 4 IST algorithm**

| Algorithm | IST iterative procedure |
|---|---|
| **Input:** | 2-D echo data $\boldsymbol{Y}$ |
| | Down-sampling matrices $\boldsymbol{\Theta}_{\mathrm{a}}$, $\boldsymbol{\Theta}_{\mathrm{r}}$ |
| | Error threshold $\varepsilon$ |
| **Initial:** | Iterative parameter $\mu$ |
| | Maximum number of iterations $I_{\max}$ |
| | Image $\boldsymbol{X}^{(0)}=0$ |
| **Repeat:** | **While** $i\leqslant I_{\max}$ and Residual $>\varepsilon$ |
| (1) | $\mathbf{W}^{(i)}=\boldsymbol{Y}-\boldsymbol{\Theta}_{\mathrm{a}}H(\boldsymbol{X})\boldsymbol{\Theta}_{\mathrm{r}}$ |
| (2) | $\Delta\mathbf{X}^{(i)}=H(\boldsymbol{\Theta}_{\mathrm{a}}^{\mathrm{T}}H(\boldsymbol{X})\boldsymbol{\Theta}_{\mathrm{r}}^{\mathrm{T}})$ |
| (3) | $\beta^{(i)}=\lvert\boldsymbol{X}^{(i)}+\mu\Delta\boldsymbol{X}^{(i)}\rvert_{k+1}/\mu$ |
| (4) | $\boldsymbol{X}^{(i+1)}=R(\boldsymbol{X}^{(i)}+\mu\Delta\boldsymbol{X}^{(i)})$ |
| (5) | Residual $=\|\boldsymbol{X}^{(i+1)}-\Delta\boldsymbol{X}^{(i)}\|_{\mathrm{F}}$ |
| (6) | $i=i+1$ |
| | **end** |
| **Output:** | Reconstructed sparse image $\hat{\boldsymbol{X}}=\boldsymbol{X}^{(i)}$ |

### 3.2 Experimental results

Based on the algorithm shown in Table 4, we select partially echo data to show its effect. The experiments are implemented in MATLAB version R2021a and on a computer with Intel(R) Xeon(R) Silver 4210R CPU 2.40/2.39 GHz two processors and an NVIDIA GeForce RTX 3080 GPU. In the experiment, the running times of MF method from 100% samples, MF method from 75% samples and $L_1$-norm regularization based sparse imaging method from 75% samples within 5 iterations are 16.62, 16.13, and 170.01 s (Fig.6), respectively, which is consistent with the analysis of computational complexity in Ref.[34].

Fig.6 shows the recovered images of scenes by MF from 100% samples, MF from 75% samples and $L_1$-norm regularization based sparse imaging from 75% samples. The image contrasts of Fig.6 are shown in Table 5. It is obvious to see that the image reconstructed by sparse algorithm has higher

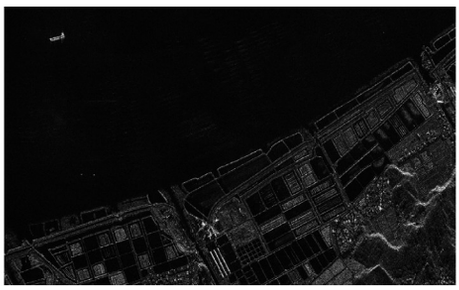

(a) MF from100% samples

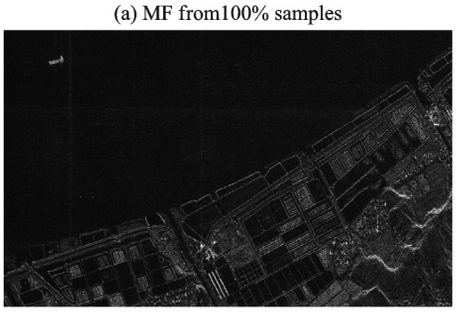

(b) MF from 75% samples

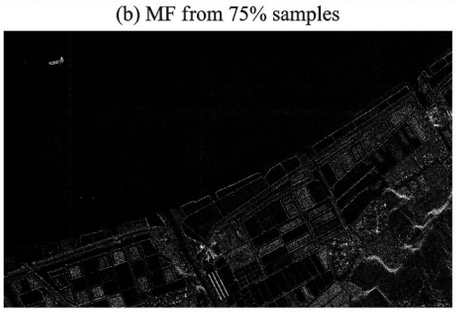

(c) $L_1$-norm regularization based sparse imaging from 75% samples

Fig.6 Reconstructed images by different methods

**Table 5 Contrast of imaging results**

| Figure | Fig.6(a) | Fig.6(b) | Fig.6(c) |
|---|---|---|---|
| Contrast | 12.403 9 | 9.024 5 | 29.817 5 |

image contrast, indicating lower sidelobes and clutter interference.

## 4 Conclusions

We apply the RDA and the parameter estimation method based on FrFT to process Fucheng-1 raw data, and then the sparse imaging algorithm is utilized to reconstruct images from down-sampled data. In the first, the theory of RDA is briefly explained. Then we introduce the parameter estimation method based on FrFT to attain accurate azimuth chirp rate. Finally, we introduce the $L_1$-norm regularization based sparse imaging algorithm. Experimental results show that the estimated parameter leads to better focusing effects of Fucheng-1 data. Besides, the sparse imaging algorithm can accurately reconstruct the down-sampled Fucheng-1 data and suppress sidelobes and clutter.

**References**

[1] HAN Y, DAI K, DENG J, et al. Fucheng-1, high-resolution Chinese interferometric SAR: First DInSAR result for landslides monitoring[J]. Measurement, 2025, 247: 116876.

[2] FENG S, DAI K, SUN T, et al. Mini-satellite Fucheng 1 SAR: Interferometry to monitor mining-induced subsidence and comparative analysis with Sentinel-1[J]. Remote Sensing, 2024, 16(18): 3457.

[3] WU Z, ZHANG W, CAI J, et al. The deformation monitoring capability of Fucheng-1 time-series InSAR[J]. Sensors, 2024, 24(23): 7604.

[4] CHANG F, LI H, DONG S, et al. Pre-, co-, and post-failure deformation analysis of the catastrophic Xinjing Open-Pit Coal Mine Landslide, China, from optical and radar remote sensing observations[J]. Remote Sensing, 2024, 17(1): 19.

[5] XIAO Ruya, WANG Xun, SUN Jingyi, et al. Comparisons of differential interferometry of Chinese SAR satellites in ground deformation monitoring[J]. Geomatics and Information Science of Wuhan University, 2025, 50(8): 1517-1526. (in Chinese)

[6] LIU Y, GUO Y, MA S, et al. Monitoring ultra high-voltage transmission tower deformation and corridor subsidence using China C-band synthetic aperture radar and Sentinel-1 data[J]. Geocarto International, 2025, 40(1): 2462482.

[7] TSAIG Y, DONOHO D L. Extensions of compressed sensing[J]. Signal Processing, 2006, 86(3): 549-571.

[8] BARANIUK R, STEEGHS P. Compressive radar imaging[C]//Proceedings of 2007 IEEE Radar Conference. [S.l.]: IEEE, 2007: 128-133.

[9] HERMAN M A, STROHMER T. High-resolution radar via compressed sensing[J]. IEEE Transactions on Signal Processing, 2009, 57(6): 2275-2284.

[10] POTTER L C, ERTIN E, PARKER J T, et al. Sparsity and compressed sensing in radar imaging[J]. Proceedings of the IEEE, 2010, 98(6): 1006-1020.

[11] ZENG J S, FANG J, XU Z B. Sparse SAR imaging based on $L_{1/2}$ regularization[J]. Science China—Information Sciences, 2012, 55(8): 1755-1775.

[12] ÇETIN M, STOJANOVIĆ I, ÖNHON N Ö, et al. Sparsity-driven synthetic aperture radar imaging: Reconstruction, autofocusing, moving targets, and compressed sensing[J]. IEEE Signal Processing Magazine, 2014, 31(4): 27-40.

[13] RAMDANI S. Compressive sensing approach for microwave imaging application[C]//Proceedings of 2018 International Conference on Signals and Systems. [S.l.]: [s.n.], 2018: 197-200.

[14] ZHANG B C, HONG W, WU Y R. Sparse microwave imaging: Principles and applications[J]. Science China —Information Sciences, 2012, 55(8): 1722-1754.

[15] YANG D, LIAO G, ZHU S, et al. SAR imaging with undersampled data via matrix completion[J]. IEEE Geoscience and Remote Sensing Letters, 2014, 11(9): 1539-1543.

[16] ZHANG Z, ZHANG B, HONG W, et al. SAR imaging of moving target in a sparse scene based on sparse constraints: Preliminary experiment results[C]//Proceedings of 2015 IEEE International Geoscience and Remote Sensing Symposium. [S.l.]: IEEE, 2015: 2844-2847.

[17] ROUABAH S, OUARZEDDINE M, SOUISSI B. Compressed sensing application on non sparse SAR images based on CoSaMP algorithm[C]//Proceedings of 2018 International Conference on Signal, Image, Vision and their Applications. [S.l.]: [s.n.], 2018: 1-6.

[18] BI H, BI G, ZHANG B, et al. From theory to application: Real-time sparse SAR imaging[J]. IEEE Transactions on Geoscience and Remote Sensing, 2020, 58(4): 2928-2936.

[19] XU G, ZHANG B, CHEN J, et al. Sparse inverse synthetic aperture radar imaging using structured low-rank method[J]. IEEE Transactions on Geoscience and Remote Sensing, 2022, 60: 5213712.

[20] KANG M S, BAEK J M. SAR image reconstruction via incremental imaging with compressive sensing[J]. IEEE Transactions on Aerospace and Electronic Systems, 2023, 59(4): 4450-4463.

[21] SONG S, DAI Y, SUN S, et al. Efficient image reconstruction methods based on structured sparsity for short-range radar[J]. IEEE Transactions on Geoscience and Remote Sensing, 2024, 62: 5212615.

[22] ZHOU G, ZUO Y, ZHANG Z, et al. CR-DEQ-SAR: A deep equilibrium sparse SAR imaging method for compound regularization[J]. IEEE Journal of Selected Topics in Applied Earth Observations and Remote Sensing, 2025, 18: 4680-4695.

[23] KANG M S, BAEK J M. Compressive sensing based Omega-K algorithm for SAR focusing[J]. IEEE Geoscience and Remote Sensing Letters, 2025, 22: 4003405.

[24] ZHANG L, HU M, WANG G, et al. Range-dependent map-drift algorithm for focusing UAV SAR imagery[J]. IEEE Geoscience and Remote Sensing Letters, 2016, 13(8): 1158-1162.

[25] XU J, PENG Y, XIA X G. Parametric autofocus of SAR imaging-inherent accuracy limitations and realization[J]. IEEE Transactions on Geoscience and Remote Sensing, 2004, 42(11): 2397-2411.

[26] LIN H, CHEN J, XING M, et al. Time-domain autofocus for ultrahigh resolution SAR based on azimuth scaling transformation[J]. IEEE Transactions on Geoscience and Remote Sensing, 2022, 60: 5227812.

[27] WANG G, ZHANG M, HUANG Y, et al. Robust two-dimensional spatial-variant map-drift algorithm for UAV SAR autofocusing[J]. Remote Sensing, 2019, 11(3): 340.

[28] EICHEL P H, JAKOWATZ JR C V. Phase-gradient algorithm as an optimal estimator of the phase derivative[J]. Optics Letters, 1989, 14(20): 1101-1103.

[29] SANTHANAM B, HAYAT M. On a pseudo-subspace framework for discrete fractional Fourier transform based chirp parameter estimation[C]//Proceedings of 2011 Digital Signal Processing and Signal Processing Education Meeting. [S.l.]: [s.n.], 2011: 360-363.

[30] LI Z, ZHANG X, YANG Q, et al. Hybrid SAR-ISAR image formation via joint FrFT-WVD processing for BFSAR ship target high-resolution imaging[J]. IEEE Transactions on Geoscience and Remote Sensing, 2022, 60: 5215713.

[31] KIM C K, PARK M Y, SHIN G H, et al. An improved technique for single-channel video-SAR based on fractional Fourier transform[J]. IEEE Transactions on Aerospace and Electronic Systems, 2022, 58(5): 4044-4052.

[32] BENNETT J R, CUMMING I G. A digital processor for the production of Seasat synthetic aperture radar imagery[C]//Proceedings of Laboratory for Applications of Remote Sensing Symposia. [S.l.]: [s.n.], 1979: 316.

[33] FANG J, XU Z, ZHANG B, et al. Fast compressed sensing SAR imaging based on approximated observation[J]. IEEE Journal of Selected Topics in Applied Earth Observations and Remote Sensing, 2013, 7(1): 352-363.

[34] BI H, LI G, SONG Y, et al. Design and performance analysis of sparse Tops SAR mode[J]. IEEE Journal of Selected Topics in Applied Earth Observations and Remote Sensing, 2022, 15: 8898-8909.

**Acknowledgements** The authors would like to thank the Spacety China for providing the Fucheng-1 SAR echo data-

set. This work was supported in part by the National Natural Science Foundation of China (No.62271248), the Natural Science Foundation of Jiangsu Province (No.BK20230090), and the Key Laboratory of Land Satellite Remote Sensing Application through the Ministry of Natural Resources of China (No.KLSMNR-K202303).

**Authors**

**The first author** Mr. **CAI Fuxuan** received the B.S. degree in information engineering from Nanjing University of Aeronautics and Astronautics (NUAA) in 2023. He is currently working toward the master degree in information and communication engineering with NUAA. His current research interests include sparse SAR mode design and SAR imaging.

**The corresponding author** Prof. **BI Hui** received the B.S. degree in electronics and information engineering from Yantai University in 2012, and the Ph.D. degree in signal and information processing from University of Chinese Academy of Sciences (UCAS) in 2017. From 2012 to 2017, he worked in the Science and Technology on Microwave Imaging Laboratory, Institute of Electronics, Chinese Academy of Sciences (IECAS), China. He was a Research Fellow with School of Electrical and Electronic Engineering, Nanyang Technological University (NTU), Singapore, from 2017 to 2018. Since 2018, he has been working in College of Electronic and Information Engineering, NUAA, where he is currently a professor. His main research interests are sparse microwave imaging with compressive sensing, synthetic aperture radar data processing and application, sparse signal processing, and 3D/4D SAR imaging.

**Author contributions** Prof. **BI Hui** designed the study. Mr. **CAI Fuxuan** contributed to echo data extract, sparse SAR imaging, imaging results analysis and the manuscript writing. Mr. **ZHU Ziyi** contributed to the Doppler parameter estimation of the study. Mr. **SONG Yufan** contributed to sparse SAR imaging. All authors commented on the manuscript draft and approved the submission.

**Competing interests** The authors declare no competing interests.

(Production Editor: WANG Jing)

# 涪城一号SAR卫星高分辨率稀疏成像及多普勒参数估计

蔡辅轩[1,2], 朱子逸[1,2], 宋宇凡[1,2], 毕 辉[1,2]

(1.南京航空航天大学电子与信息工程学院,南京 211106, 中国; 2.南京航空航天大学雷达成像与微波光子学教育部重点实验室, 南京 211106, 中国)

**摘要:**近年来国内商用合成孔径雷达(Synthetic aperture radar, SAR)发展迅速,有多颗商用SAR卫星已经在轨运行,且在灾害监测、自然资源管理和形变观测等方面显示出巨大潜力。涪城一号是中国天仪研究院研制的第一颗提供干涉SAR(InSAR)服务的C波段商用SAR卫星,这标志着中国遥感数据服务逐步走向成熟。本文对涪城一号采集的原始数据进行研究,首先对距离-多普勒算法进行介绍;然后阐述基于分数阶傅里叶变换的参数估计原理,实现了方位调频率的精确估计,从而有效提高了成像质量;最后,利用基于$L_1$范数正则化的稀疏成像方法从降采样数据中重建图像。实验结果表明,该稀疏成像算法能够准确重构欠采样的涪城一号数据,并抑制旁瓣和杂波。

**关键词:**涪城一号;合成孔径雷达;稀疏合成孔径雷达成像;参数估计